PHYSICAL REVIEW E **72**, 015401(R) (2005)

Hot-electron surface retention in intense short-pulse laser-matter interactions

R. J. Mason,* E. S. Dodd,† and B. J. Albright‡
Los Alamos National Laboratory, Los Alamos, New Mexico 87545, USA
(Received 10 November 2004; published 25 July 2005)

Implicit hybrid plasma simulations predict that a significant fraction of the energy deposited into hot electrons can be retained near the surface of targets with steep density gradients illuminated by intense short-pulse lasers. This retention derives from the lateral transport of heated electrons randomly emitted in the presence of spontaneous magnetic fields arising near the laser spot, from geometric effects associated with a small hot-electron source, and from *E* fields arising in reaction to the ponderomotive force. Below the laser spot hot electrons are axially focused into a target by the *B* fields, and can filament in moderate *Z* targets by resistive Weibel-like instability, if the effective background electron temperature remains sufficiently low. Carefully engineered use of such retention in conjunction with ponderomotive density profile steepening could result in a reduced hot-electron range that aids fast ignition. Alternatively, such retention may disturb a deeper deposition needed for efficient radiography and backside fast ion generation.

DOI: 10.1103/PhysRevE.72.015401 PACS number(s): 52.35.Mw, 52.25.Dg, 52.65.−y

Ten years ago, researchers first proposed [1] the use of an ultraintense ($>10^{19}$ W/cm^2) short-pulse laser (at 1 μm) as a "fast ignitor" for inertial confinement fusion (ICF). Hot electrons produced by laser absorption near the critical surface of a precompressed deuterium-tritium (DT) pellet (at roughly 300 g/cm^3) would transport through the depth of an alpha particle range, $\rho R_{\mathrm{alpha}} \sim 0.3$, to ignite thermonuclear burn. Alternatively, such electrons might spread to the rear of a thin, moderate *Z* foil to launch focused fast ions for deposition near the surface of a subsequent DT target [2]. In addition, short-pulse deeply driven fast electrons were proposed as an intense *K*-alpha source for ICF radiography.

Preliminary fast ignition experiments have, indeed, shown increased neutron yield, particularly when a high-*Z* cone [3] was used to direct short-pulse-generated hot electrons toward a precompressed target, implying useful hot-electron deposition in the DT. Present indications are that short-pulse-initiated fast electrons can launch significant fast ion beams from the rear side of thin foils [4]. Preparatory $K\alpha$ experiments for radiography have shown that in aluminum foil targets hot electrons spread out in a fanlike expansion [5] from the laser deposition point. Meanwhile, spectroscopic data from CH foil experiments with buried Al layers have shown rings with the largest diameters at the shallower depths, while $K\alpha$ imaging techniques on Al foils (with Cu) have shown a strong spreading of transport near the entry surface and a rapid axial attenuation [6], possibly suggesting an extended surface presence of hot electrons.

This paper shows computationally that a significant fraction of the isotropically emitted hot electrons *from a short-pulse laser* can be retained near a target's surface by the action of self-consistent magnetic fields, small spot geometry, and ponderomotive *E* fields. Further, we demonstrate magnetic focusing of axially penetrating hot electrons below the laser spot, and we attribute filamentation to the presence of background resistivity. Collectively, these effects may affect the signature of short-pulse targets as radiography and fast ion sources, and reduce the deep deposition of hot-electron energy needed for effective radiography. Alternatively, in coordination with profile modification from ponderomotive influences allowing deposition at high densities, such retention could enhance coupling to the background plasma, as an aid to fast ignition.

Model problem. In our simulations $\lambda = 1.06$ μm wavelength light strikes an aluminum foil over picosecond time scales. The foil is taken as initially solid and partially ionized with an effective *Z* of 3. We look in two-dimensional (2D), Cartesian geometry at foils 160-μm wide and 130-μm thick. The incident intensity rises artificially in 1 fs to a constant 4×10^{19} W/cm^2. The beam is normally incident with a Gaussian profile of 8 μm full width at half maximum (FWHM). Facing the laser the electron density rises exponentially over 16 μm from our void value of 10^{16} cm^{-3} to a peak value of 1.5×10^{23} cm^{-3}, or to 150 times the critical density n_{crit}. The electron and ion background temperatures are initially set at 10 eV. This matches recent experiments [5,6].

Approach. Traditional explicit particle-in-cell (PIC) codes [7] would require more than 10^7 particles, 12 000 cells on a side, and initial kilovolt background temperatures (or find lower initial temperatures rising through finite grid instability to that level). We use the implicit PIC/multifluid hybrid code ANTHEM [8], typically employing a simple 100×100 cell mesh, temperatures in the physical eV range, and rarely more than 4×10^5 particles. Implicitness avoids numerical electrostatic grid instability. Here, the background plasma is modeled as a coupled pair of Eulerian ion and cold-electron fluids, while the hot electrons are treated as a collection of emitted PIC particles. Both electron components are relativistic and coupled at a modified Spitzer collisional rate to the ions. The hot-electron particles undergo Rutherford scattering off the ions, and drag against the background cold electrons. Our time step is set by a Courant condition on the electrons for stability, with an additional Δt constraint on

*Also at: Research Applications Corporation, Los Alamos, NM 87544. Electronic addresses: mason@lanl.gov and rodmason01@msn.com
†Electronic address: esdodd@lanl.gov
‡Electronic address: balbright@lanl.gov

momentum increments in the E field for accuracy.

Electromagnetic fields are determined by the implicit moment method [9], here restricted to E_x and E_y electric fields in the plane of the electron currents, and B_z out of it. Accordingly, in updating the $\boldsymbol{E}$ fields,

$$\frac{\partial \vec{E}}{\partial t} = -4\pi e(Zn_i\vec{v}_i - n_e\vec{v}_e) + c\vec{\nabla}\times\vec{B},$$

$$v_\alpha = u_\alpha/\gamma_\alpha, \quad n_e v_e = \Sigma n_\alpha v_\alpha, \quad \alpha = h,c \tag{1}$$

with α designating hot or cold electrons, we use a set of auxiliary fluid moment equations,

$$m_e\frac{\partial\, n_\alpha\vec{u}_\alpha}{\partial\, t} = -\vec{\nabla}\cdot\bar{P}_\alpha - en_\alpha\left(\vec{E} + \frac{\vec{v}_\alpha x\ \vec{B}}{c}\right)$$

$$-\frac{\omega_{p\alpha}^2}{2c\omega^2\gamma_\alpha}\frac{[n_r,n_{\rm crit}]_{\rm min}}{n_r}\vec{\nabla}I - C_a\gamma_\alpha m_e n_\alpha(\vec{v}_\alpha - \vec{v}_i), \tag{2}$$

plus a similar equation for the ions to predict future source currents, based themselves on time-centered and advanced electric fields. Here, $\boldsymbol{p}_\alpha = m_0\boldsymbol{u}_\alpha$ is the relativistic electron momentum, m_0 is the rest mass, $\gamma=(1+u^2/c^2)^{1/2}$ is the Lorentz factor, and $\vec{\nabla}\cdot\bar{P}_\alpha$ includes the static and dynamic pressure terms. Also, C_α is the collision rate for each electron component with the ion background, $\omega_{p\alpha}$ is the species plasma frequency, and ω is the frequency of the incident light. Faraday's law, $\partial\boldsymbol{B}/\partial t = -c\vec{\nabla}\times\boldsymbol{E}$, then gives a predicted $\boldsymbol{B}$ field consistent with $\boldsymbol{E}$, after iteration of the resultant elliptic system for B_z. Both the real and the auxiliary electron fluid momentum equations, and the particle electrons equations are updated with the mass-scaled momentum $\boldsymbol{u}$ in the $\boldsymbol{u}\times\boldsymbol{B}/(\gamma c)$ term treated implicitly. This assures stable $\boldsymbol{E}\times\boldsymbol{B}$ drift of electrons in strong-field regions. Particle currents are determined from a continuity preserving Buneman algorithm. Once the fluid and/or particle components have been moved in a time step, the difference between the real currents and predicted currents is used as a correction to the predicted current in Ampere's law for the next cycle.

Normally-incident light is transported across the mesh by a grid-following algorithm, much as used in ICF hydrodynamics codes. Its intensity represents an average of the oscillating $\boldsymbol{E}$ and $\boldsymbol{B}$ fields of the wave. Its evolution could, in principal, be calculated in the near vacuum outside a target, as part of the implicit field determination, but this would require a mesh with at least, six cells per wavelength, much finer than used here, and correspondingly smaller time steps. The light's energy is deposited in the first cell above critical. From the deposited energy we launch hot electrons as PIC particles in a relativistic distribution as either a Maxwellian or a momentum shell with a mean Lorentz factor $\langle\gamma_h\rangle$ and temperature related by $T_h=(\langle\gamma_h\rangle^2-1)mc^2/(3\kappa\langle\gamma_h\rangle)$. From earlier PIC simulations [10] we set the temperature T_h at 1.8 MeV, and the absorption fraction at 27% for the applied $I=4\times10^{19}$ W/cm^2. The rest of the light is reflected, but adds to the local intensity I, with $\vec{\nabla}I$ used to determine the ponderomotive force (PMF) and the light momentum transferred to a target. A limiting density factor, $D_f=[n_r/n_{crit}]/n_r$, in which n_r is the relativistically corrected density, $n_h/\gamma_h + n_c/\gamma_c$ (that was missing in Ref. [11]), multiples $\vec{\nabla}I$ to assure that near steep density gradients no density higher than the relativistic critical value is accelerated by the PMF. Each of our calculations required about 2–3 h CPU time on a single, 2 GHz PC processor.

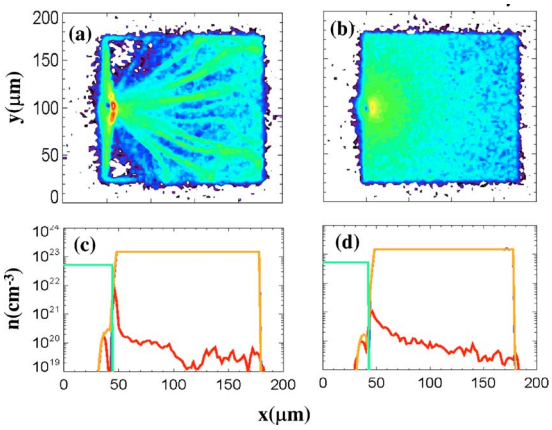

FIG. 1. (Color online) Hot-electron density contours and cuts for 1 ps with (a,c) B field "on" and (b,d) $B=0$. Laser from left. Ion (trapezoidal) and overlaid cold-electron density and hot-electron density, n_h (jagged). Near the surface in (a,c) n_h is 10 times larger with B field "on," where, also, surface transport and filamentation are evident.

Results. Figure 1(a) shows the hot-electron density n_h in our aluminum foil after 1 ps. The laser-facing surface of the foil was initially at $x=50$ μm. The left and right problem boundaries were absorbing, the top and bottom boundaries were reflecting. Particle hot-electron emission in the fixed momentum shell was employed. The hot electrons have penetrated fully to the back of the foil and broken into streamers emanating from their source. The envelope of streamers is conical, in agreement with recent experiments [5]. Our streamers show little tendency to pinch together. Along the surface opposing vertical streamers identify a lateral flow of hot electrons, which turn at the foil's edges to continue towards its back. The hot-electron density is very high within ±20 μm of the spot center. This accumulation matches the bright central emission feature also reported in recent experiments [6]. Between each surface streamer and the conical envelope is a hot-electron void. Hot electrons must enter the target under the spot center. The cone of filaments is seen as early as 350 fs, with gentle disturbances beginning at the leading edge of the expanding hot-electron cloud, which break first into fingers and later into the lengthy filaments. These structures are even more pronounced when relativistic Maxwellian emission with its spread of speeds is employed. On our time and spatial scales there is little evident ion density imprint at the laser surface of the foil. The Fig. 1(c) central density cut (at $y=100$ μm) for our particle calculation shows a peak hot-electron density near 8×10^{21} cm^{-3}, dropping over roughly ~10 μm to 10^{20} cm^{-3}, and then again to 10^{19} cm^{-3} over the next 50 μm (as it crosses a trough between the filaments); n_h returns to nearly 10^{20} cm^{-3} to the back of the foil. A sharp density spike near the deposition point is recurrent in all our simulations employing isotropic emission of the hot electrons.

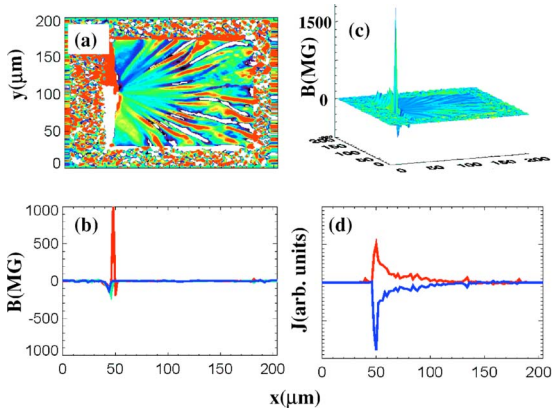

FIG. 2. (Color online) (a) B_z-field contours at 1 ps with (b) calibrating cut at $y=100$ μm. To the left near the laser B_z exceeds 10^3 MG. Inside the target the B field in filaments is only ~ 5 MG. (c) Surface plot of B_z, showing spikes near laser spot. (d) Corresponding outgoing (above) hot-electron flux, and return cold-electron flux (below) in arbitrary units.

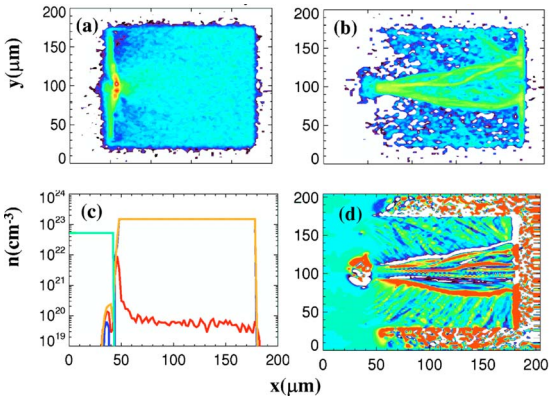

FIG. 3. (Color online) Hot electron foil penetration at 1 ps, with B-field inclusion but zero resistivity, showing (a) little filamentation but (c) significant surface accumulation. Electrons launched from beneath the surface with resistivity and B field included, showing (b) no laser surface retention but backside density accumulation and (d) B_z-field generation plus filamentation (bottom-most filament is positive B_z).

If, alternatively, the magnetic field is suppressed by going to the electrostatic limit [setting $B \equiv 0$ in Eq. (2) and the fluid/particle updates, while ignoring Faraday's law], we see at 1 ps, Fig. 1(b), nearly isotropic spreading of the hot electrons into the target and no notable surface transport. The hot-electron density spikes at a much lower $\sim 10^{21}$ cm^{-3} near the deposition point, and drops roughly like $1/r^2$ out to $x=180$ μm, consistent with semicylindrical dispersal. A noisy particle hot-electron density field, but no filamentation, is observed.

Further results from the full problem, again including B field, scattering, and drag are collected in Fig. 2. Frame (a) gives a plot of the B-field intensity. At the target surface the field is above 10^3 MG, as indicated by the $y=100$ μm central cut of Fig. 2(b). Frame (c) shows a surface plot of the B field, showing its relatively intense spikes at the laser spot. Within the foil low-level ±5 MG field magnetic streamers are correlated with the hot density filamentary structures. The cold background electron temperature field (not shown) exhibits similar structures, due to joule heating of the returning electrons attempting to neutralize the hot-electron flow. Figure 2(d) shows a $y=100$ μm cut of the nearly balanced, counterstreaming hot- and cold-electron fluxes.

Next, when the physical B field is restored, but all the electron scattering and drag is suppressed, the surface hot-electron retention and vertical (lateral transport) returns as shown in Figs. 3(a) and 3(c), but the internal filamentation absent. This is also true if Rutherford scattering and drag on the hot electrons is retained, while only the cold collisionality (resistivity) is suppressed. On this spatial scale, therefore, cold collisionality is needed for the filamentation, i.e., it is the product of a resistive Weibel-like instability [12]. The hot-electron density at the laser spot is, in fact, higher, i.e., 5×10^{22} cm^{-3}, than in the collisional case, but it drops to a lower 10^{20} cm^{-3} within 15 μm of the surface. So, the hot collisions add some diffusion into the target of the trapped surface electrons, otherwise localized by the B field.

The resistivity of metals such as aluminum rises as the background temperature drops from kilovolt values down to the neighborhood of 100 eV. Below this to 10 eV the physical resistivity can be flat and even dropping [13], unlike Spitzer. To check the consequences of such relatively reduced resistance on short-pulse filamentation, we reran the Figs. 1(a) and 1(c) simulation with caps set on the maximum resistivity corresponding to lower limits set on the background temperature going into the Spitzer formula. With the cap fixed at 30 eV the results essentially reproduce Fig. 1(a). At 100 eV the filaments are half as wide, in the same cone, but mainly radial. Finally, with a 300-eV cap, we see a smeared result, as in Fig. 1(b), and virtually no filamentation. From this we conclude that significant filamentation should be seen in corresponding Al experiments where the actual resistivity at 10–100 eV is less than the Spitzer values.

Most of our runs were made for a fixed *average* hot-electron temperature set by the laser [10]. However, to explore limited effects from hot-electron variation across the spot, we reran our model problem with the hot-electron temperature set at two times the average value beyond the FWHM point in the laser spot, while inside this point our electrons were emitted at half that average. Generally, the Fig. 1(a) phenomenology was reproduced, but at any given time the hot-electron filaments went deeper, and the surface retention was greater. The general Fig. 1(a) scenario was also obtained when the wings of the spot were 1/2 the central temperature.

Alternate implicit studies [14] have injected hot electrons as an electron beam into laser targets. When we do this, simply launching the hot electrons with the same 8 μm FWHM intensity profile into an initial 3° cone from a plane 4-μm below the critical surface, we find no lateral surface transport. This matches the earlier studies. Our beam first propagates about 100 μm undisturbed. Thereafter, it filaments, spreads, and grows to a width of 70 μm upon reaching the foil's backside. The resultant 1 ps density profile is shown in Fig. 3(b) with related B fields in frame (d). When the beam is launched with only 1° divergence, it establishes a distinct back-surface B field of 100 MG, similar to very early CO_2 laser predictions [15]. This field then propagates

out to the foil corners at its top and bottom, and then along these surfaces back toward the laser.

Surface B fields have well-known [15,16] thermoelectric origins, and are similar to those seen in very early CO_2 experiments [17], but here they are rising on a 10^3-fold shorter time scale. At the front target surface the net electron component has a density gradient in the laser (x direction) and an average temperature gradient in the y direction. So, in Faraday's law the curl of $E \sim -\vec{\nabla} P/en$ (with $P=n\kappa T$) from Eq. (2) generates the B_z field. If the hot electrons are somehow excluded from the surface (as with the internal launch of a narrow beam), this field source should be negligible. When, however, the beam emission angle is increased to as little as 45°, we have found (in other simulations) that a significant number of hot electrons scatter back toward the front, where then their temperature and density gradients can establish a front-surface B field, particle retention, and lateral transport.

Under the laser spot the ponderomotive force pushes both the hot- and cold-electron components into the foil until they are stopped by the charge separation E field that pulls on the ions. Our density limited PMF force is properly weaker here than previously employed [11]. Still, it impedes the ion blowoff, thereby confining the lateral transport more closely to the surface. If we suppress this force, the lateral spread of the hot component is 10% greater by 1 ps. We have run the model, Fig. 1(a) problem with 200 lateral cells and $\Delta y = 1.0$ μm, and found no significant change in the results. We have further checked implicit ANTHEM in the near-critical region, using $\Delta x = \Delta y = 0.1$ μm, by comparison with Los Alamos National Laboratory's version of the parallel explicit code TRISTAN [18], and with published results from Livermore's ZOHAR model [19]. In each calculation similar weak critical surface Weibel-like instabilities are evident. For the higher densities reported here ANTHEM [8] has shown little collisionless Weibel; this is also supported by recent full PIC calculations [7]. Further studies at high resolution are under way and will be reported elsewhere. These have not shown any significant change in the interplay of surface transport and resistive filamentation indicated here. Our foil is not at sufficiently low density or under high enough intensity for relativistic alteration of the critical density to lead to target penetration by the light, as seen by others [20,21]. Nor does our deposition scheme allow for transport of the light harmonics.

Our simulations have not shown a pinching of the hot-electron beam launched by the short-pulse laser, but our hot-electron beam is centrally directed. Despite lateral transport losses, the magnetic field and PMF act to concentrate hot-electron energy near the laser spot. This could possibly benefit fast ignition if through density profile modification the laser light could be deposited below a steep high-density interface in compressed DT fuel. Filamentation of the electron beam as it passes through a thick foil may degrade its use as a smooth and uniform backside driver of ions. This would occur since the hot filaments would act to preferably produce fast ions at their points of contact on a foil's backside. But multiple surface reflections in thin foils (<10 μm) should act to restore a smooth ion drive. This distinction in ion source quality has been seen experimentally [22]. In the radiographic application of short-pulse targets, we must now anticipate a signature from electrons both confined on the surface and expanding conically beneath it by the action of intense self-magnetic fields.

We thank M. Key, R. Freeman, R. Stephens, D. Barnes, J. Fernández, J. Cobble, and M. Hegelich for helpful discussions. This work was performed under the auspices of the U.S.D.O.E.

[1] M. Tabak *et al.*, Phys. Plasmas **1**, 1626 (1994);S. Atzeni, *ibid.* **6**, 3316 (1999).
[2] M. Roth *et al.*, Phys. Rev. Lett. **86**, 436 (2001).
[3] R. Kodama *et al.*, Nature (London) **412**, 798 (2001);R. Kodama, *ibid.* **418**, 933 (2002);Y. Sentoku *et al.*, Phys. Plasmas **11**, 3083 (2004);R. B. Campbell, R. Kodama, T. A. Melhorn, K. Tanakas, and P. R. Welch, Phys. Rev. Lett. **94**, 055001 (2005).
[4] S. P. Hatchett *et al.* Phys. Plasmas **7**, 2076 (2000);E. L. Clark *et al.*, Phys. Rev. Lett. **84**, 670 (2000);R. A. Snavely *et al. ibid.* **85**, 2945 (2000);M. Hegelich, *et al. ibid.* **89**, 085002 (2002).
[5] R. Freeman *et al.*, J. Quant. Spectrosc. Radiat. Transf. **81**, 183 (2003);R. Stephens *et al.*, Phys. Rev. E **69**, 066414 (2004).
[6] J. A. Koch *et al.*, Phys. Rev. E **65**, 016410 (2002);M. Key *et al.*, in *IFSA Proceedings* p. 353 (2003).
[7] C. Ren *et al.*, Phys. Rev. Lett. **93**, 185004 (2004).
[8] R. J. Mason and C. W. Cranfill, IEEE Trans. Plasma Sci. **PS-14**, 45 (1986);R. J. Mason,J. Comp. Physiol. **71**, 429 (1987).
[9] R. J. Mason, J. Comput. Phys. **41**, 233 (1981);R. J. Mason, *ibid.* **51**, 484 (1983);R. J. Mason, in *Multiple Time Scales*, edited by J. U. Brackbill and B. I. Cohen (Academic, New York, 1985), p. 233.
[10] S. C. Wilks *et al.*, Phys. Rev. Lett. **69**, 1383 (1992).
[11] R. J. Mason and M. Tabak, Phys. Rev. Lett. **80**, 524 (1998).
[12] J. M. Wallace *et al.*, Phys. Fluids **30**, 1088 (1987).
[13] H. M. Milchberg *et al.*, Phys. Rev. Lett., **61**, 2364 (1988);R. R. Freeman *et al.*, in *Proc. of the 3rd Int. Conf. on Inertial Fusion Sciences and Applications*, IFSA (Monterey, 2003), (2004 Amsterdam Nuclear Society), p. 465.
[14] D. R. Welch *et al.*, in *IFSA Proceedings* p. 398 (2003);P. A. Norreys *et al.*, Phys. Plasmas **11**, 2746 (2004).
[15] R. J. Mason, Phys. Rev. Lett. **42**, 239 (1979).
[16] D. W. Forslund, and J. U. Brackbill Phys. Rev. Lett. **48**, 1614 (1982).
[17] M. A. Yates *et al.* Phys. Rev. Lett. **49**, 1702 (1982).
[18] E. S. Dodd *et al.*, Phys. Rev. E **70**, 056410 (2004).
[19] S. Wilks *et al.*, Phys. Plasmas **8**, 542 (2001).
[20] A. Pukhov and J. Meyer-ter-Vehn, Phys. Rev. Lett. **79**, 2686 (1997).
[21] B. Lasinski *et al.*, Phys. Plasmas **6**, 2855 (1999).
[22] R. A. Snavely (private communication).